Available online at www.sciencedirect.com
SCIENCE DIRECT®
Nuclear Instruments and Methods in Physics Research A 496 (2003) 198–214
NUCLEAR INSTRUMENTS & METHODS IN PHYSICS RESEARCH Section A
www.elsevier.com/locate/nima

Charge state studies of low energy heavy ions passing through hydrogen and helium gas

W. Liu[a], G. Imbriani[b], L. Buchmann[c], A.A. Chen[a,1], J.M. D'Auria[a,c,d,*], A. D'Onofrio[e], S. Engel[f], L. Gialanella[b], U. Greife[g], D. Hunter[a], A. Hussein[h], D.A. Hutcheon[c], A. Olin[c,h], D. Ottewell[c,i], D. Rogalla[f], J. Rogers[c], M. Romano[b], G. Roy[j], F. Terrasi[e]

[a] *Chemistry Department, Simon Fraser University, 8888 University Drive Burnaby, BC, Canada V5A 1S6*
[b] *Dipartimento di Scienze Fisiche dell 'Università di Napoli Federico II and INFN, Napoli, Italy*
[c] *TRIUMF, Vancouver, BC, Canada*
[d] *WSNL, Yale University, New Haven, CT, USA*
[e] *Dipartimento di Scienze Ambientali della Seconda Università di Napoli, Caserta and INFN, Napoli, Italy*
[f] *Ruhr-Universität, Bochum, Germany*
[g] *Colorado School of Mines, Golden, CO, USA*
[h] *University of Northern British Columbia, Prince George, BC, Canada*
[i] *University of Victoria, Victoria, BC, Canada*
[j] *University of Alberta, Edmonton, Alberta, Canada*

Received 21 May 2002; accepted 9 July 2002

Abstract

Studies of the charge state distribution of low energy ($<1.5\,\mathrm{MeV}/u$), low Z (<13) heavy ions passing through hydrogen and helium gas of varying target pressure have been performed using separate windowless gas target systems at TRIUMF and the University of Naples. Semi-empirical relationships have been deduced to estimate the equilibrium charge state distributions as a function of beam energy. From these distributions, cross-sections for the relevant charge changing reactions have been deduced.

PACS: 34.50

Keywords: Charge state distributions; Gases; Low energy heavy ions; DRAGON

1. Introduction

The distribution of charge states that results when a heavy ion passes through matter is of interest for a number of applications including nuclear physics, gas filled recoil separators, and accelerator designs. While many related studies

*Corresponding author. Address for correspondence: Chemistry Department, Simon Fraser University, 8888 University Drive, Barnaby, BC, Canada V5A 1S6. Tel.: +1-604-291-4607; fax: +1-604-291-3765.
E-mail address: dauria@sfu.ca (J.M. D'Auria).
[1] Present address: Department of physics, McMaster University, Kingston, Ontario, Canada

0168-9002/03/$ - see front matter
PII: S0168-9002(02)01629-7

have been performed, nevertheless, few studies are available involving low energy, low Z heavy ions moving through gas. In situations in which a device only accepts a single charge state, this is an important contribution to the device acceptance.

We report herein a study of the charge state distributions resulting from the passage of heavy ions through a gas. These studies are relevant to a new facility located at the new TRIUMF-ISAC Radioactive Beams facility in Vancouver, Canada. This facility is called DRAGON (Detector of Recoils And Gammas Of Nuclear reactions) and consists of a windowless, differentially pumped, gas target coupled to a recoil mass separator to separate reaction products from incident beam, followed by a series of charged particle detection systems to detect and identify the resultant heavy ions. Further description of the full DRAGON facility can be found elsewhere [1–3]. The fusion reactions to be studied are of interest to nuclear astrophysics and involve low A ($A<30$) projectiles in the energy range of interest from 0.15 to 1.5 MeV/u.

A windowless, gas target is preferred to a hydrocarbon or adsorbed helium solid target because it gives higher yield with less background for the low yield, narrow resonance reactions of interest. Furthermore, a gas target is thin (approximately10^{18} atoms/cm^2), uniform, stable over long periods of irradiation, and essentially indestructible.

The overall detection efficiency of DRAGON depends upon the transmission of a single charge state from the charge state distribution produced in the gas target. This distribution results both from the reaction itself and the further passage of the reaction products through the gas target. The fraction of a particular charge state is a parameter that must be known to perform an absolute measurement of cross-sections as it determines the overall detection efficiency. Further, if the charge state distribution has not reached equilibrium given the gas pressure utilized, the beam energy and the effective length of the chamber, the charge state distribution as a function of thickness and initial projectile charge state distribution has to be measured. Given the paucity of data [4–7] on the charge distribution resulting from passage of the low energy, low Z ion beams through hydrogen and helium gas, studies were performed to measure these for the energy range of interest and are reported herein.

The experimental studies described herein utilized the facilities located at the University of Naples, Italy, and at the TRIUMF laboratory in Vancouver, Canada.

2. Description of the experimental setups

2.1. NABONA in Naples

2.1.1. Overview

Initial studies were performed using the NABONA (Napoli Bochum Nuclear Astrophysics Collaboration) windowless gas target system coupled to their 3 MV Tandem accelerator. Details of this system can be found elsewhere [8–10].

The charge state distributions of ^{16}O and ^{23}Na beams passing through a windowless gas target with an effective target length of 376 mm, longer than at the DRAGON facility, have been measured. A schematic diagram of the facility with details of the target provided in the inset is displayed in Fig. 1. Positive ions of certain charge states were selected by the 90° analyzing magnet, and then focused by a quadrupole doublet onto the center of the gas target. The resultant ion beam exiting the target is transported through a 30° switching magnet. The use of a post stripper (carbon foil, 5 μg/cm^2) at the object slits just before the analyzing magnet allowed the production of a wide range of beam charge states with the same energy. Electron suppressed, Faraday cups (FC) positioned before and after the gas target, and after the switching magnet, were used to measure the intensity of the passing beams. FC3 measured the total intensity of the incident beam charge states, FC4 measured the beam current (mixture of several charge states) exiting the target, and FC5 provided the intensity of a selected charge state. The vacuum in the beam line (with no gas in the gas target) was of the order 10^{-6} mbar near the target. The intensity of the transmitted charge

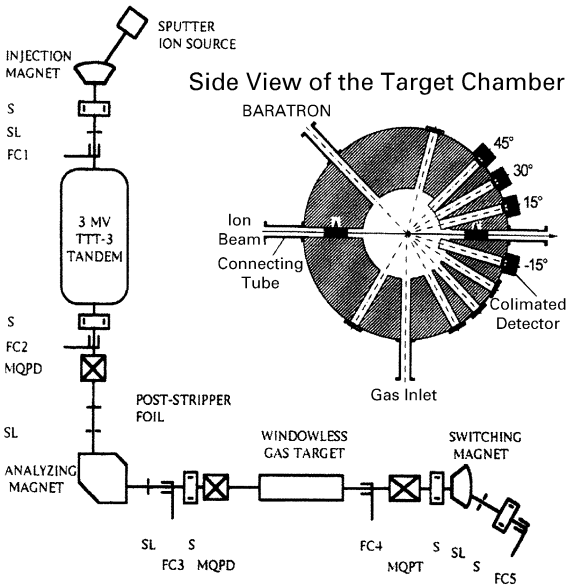

Fig. 1. Beam system at the University of Naples with the side view of the disk-shaped target chamber [10] ($S = X - Y$ steerers, SL = slits, FC = Faraday cup, MQPD = magnetic quadrupole doublet, MQPT = magnetic quadrupole triplet).

states was measured for values of the gas target pressure and for different heavy ion beams.

2.1.2. Gas target system

At Naples the windowless, NABONA gas target is run in a flow-through mode and the pressure in the chamber is measured by a baratron capacitance manometer to an accuracy of 4%. The disk shaped chamber has an outer radius of 175 mm, and the distance between the centers of apertures A and A' is 248 ± 2 mm. Further details can be found elsewhere [8–10]. Using the $p(^7\mathrm{Li},\gamma)^8\mathrm{B}$ reaction, the target pressure profile was determined to be constant inside the central chamber with a fast drop beyond its apertures. The effective target length was determined to be 376 ± 8 mm [10]. The target thickness can be calculated from the ideal gas law using

$$x = N_A LP/(RT) \tag{1}$$

$$= 2.46 \times 10^{16}\, L(\mathrm{cm}) P(\mathrm{mbar}) \ [\mathrm{molecules/cm^2}] \tag{2}$$

$$= 3.24 \times 10^{16}\, L(\mathrm{cm}) P(\mathrm{Torr}) \ [\mathrm{molecules/cm^2}] \tag{3}$$

where N_A is Avogadro's number, L the effective length of the inner gas cell, P the pressure in the cell, R the gas constant and T the temperature in the cell (assumed to be constant at 25°C).

2.2. The DRAGON facility

2.2.1. Overview

Studies of the charge state distributions for projectiles exiting the DRAGON gas target were performed using stable heavy ion beams accelerated with the new ISAC accelerator located at TRIUMF [11,12]. An off-line ion source injects beams of 2 keV/u into the LINAC accelerator, which is composed of an initial RFQ (Radio Frequency Quadrupole) accelerator, followed by a stripper system (between two 45° magnetic dipoles) and then a standard room temperature DTL (Drift Tube LINAC). Beams with $A < 30$ of energies from 0.15 to 1.5 MeV/u are available for studies. More detailed information can be found elsewhere [11,12]. DRAGON receives the beam following an achromatic bend section (two 22.5° magnetic dipoles) and various focusing devices as shown in Fig. 2. The vacuum in the upstream beam line is $< 2 \times 10^{-6}$ Torr.

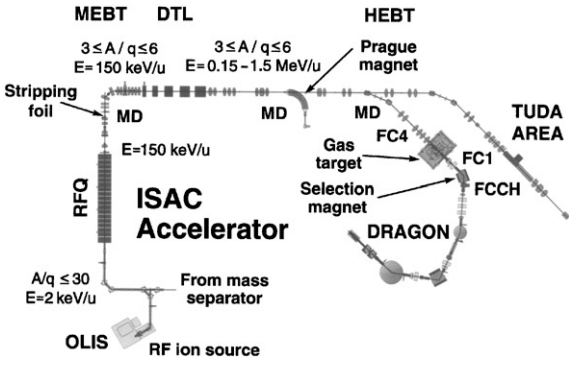

Fig. 2. Layout view of the ISAC accelerator at TRIUMF, located in Vancouver, Canada (FC = Faraday cup, MD = magnetic dipole, RFQ = radiofrequency quadrupole LINAC, DTL = drift tube LINAC, OLIS = off-line ion source, MEBT and HEBT are medium and high-energy beam transport systems).

Isotopic heavy ion beams of the desired energy and charge state were delivered to DRAGON with typical intensities of 10–100 enA. The observed transmission of the incident charge state through an evacuated target cell is $>98\%$. Studies of the charge state distribution were performed again using a FC (FC4) upstream of the target, a FC (FC1) after the target, and after a charge selecting 50° magnetic dipole (FCCH). The outputs of the FCs were integrated by the current integrators set at 10^{-10} C/pulse. The complete charge state distribution was observed by scanning the magnetic dipole, following tuning at the first two quadrupoles. Again, measurement of several pressures was performed at each energy.

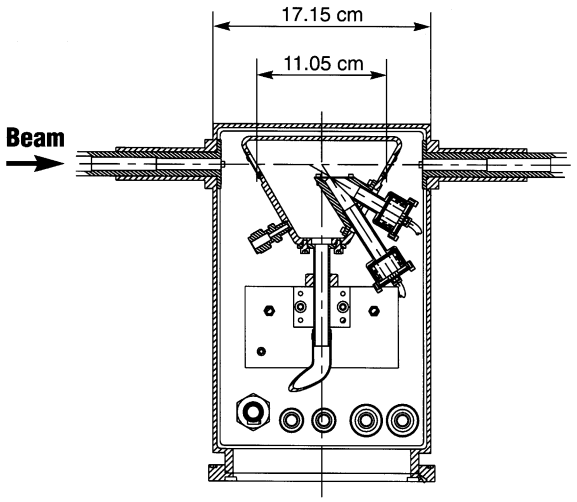

Fig. 3. Detailed view of the DRAGON inner gas target chamber.

2.2.2. Target system

The extended gas target system consists of a central, trapezoidal, inner target cell (Fig. 3) with its pumping system, and in addition, three stages of differential pumping upstream and downstream. The pumping system consists of a combination of 5 Roots blowers, 7 turbo pumps and a large mechanical pump. The inner gas target chamber has a geometrical length of 11.05 cm and can be operated at a maximum pressure of 6 Torr. Apertures of 6 mm upstream and 8 mm downstream result in a restricted gas flow (0.3 atm l/s) out of the cell. Outside of the target chamber, pressure reduction was achieved (in these studies) by a series of small diameter tubes separating further pumping stages with dimension shown in Fig. 4. Turbo-molecular pumps (V 1000 HT) on the differential stages reduce the end pressures to 1×10^{-6} Torr; this was only achieved for hydrogen when a trapezoidal shape was introduced [3].

In these measurements the DRAGON gas target operated without a cryotrap. To limit accumulation of gas impurities ($<5\%$) in this recirculation mode, the gas was refreshed every 4 h.

A more complete and detailed description of the gas target including operating parameters can be found elsewhere [3].

In order to have a quantitative measure of the beam passing through the gas target, solid state Si detectors were installed at fixed angles of 30° and 57° to monitor scattering events. The detectors do not observe the same path length in the chamber due to structural constraints. An alpha source is

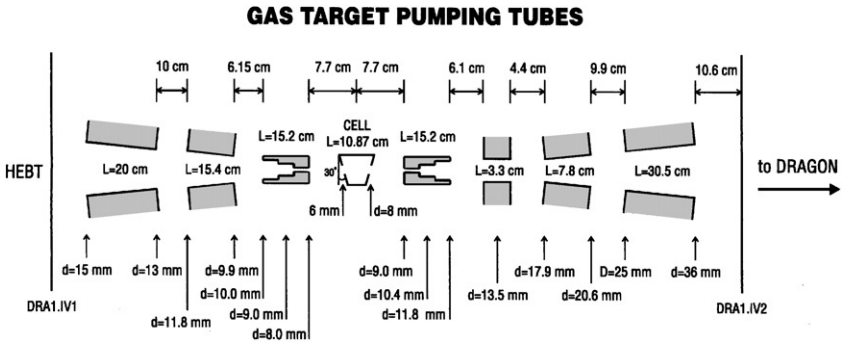

Fig. 4. Details of the inner apertures of gas target system used in the present study.

mounted permanently in a position that is visible to the 57° detector. In addition, there is also a temperature measuring device in the chamber. The pressure in the chamber is measured to 4% using a capacitance manometer.

In separate studies of the energy loss as a function of gas pressure, the effective length of the gas target was determined to be 12.3 ($\pm$0.5) cm [3].

3. Experimental results and discussion

3.1. Results and uncertainties

A selection of some of the data (fractional charge states as a function of pressure) obtained at both laboratories are displayed in Figs. 5 and 6 while the complete set of results are available upon request [13].

Table 1 presents the equilibrium charge state distributions measured at Naples for O and Na, and at ISAC for N, O and Mg beams with a variety of incident energies and incident charge states. These were extracted from the data above using a least-squares analysis.

Reproducibility of the equilibrium charge state distribution has been checked by comparing the result of ^{16}O beam of 0.325 and 0.500 MeV/u passing through a hydrogen target at Naples and Dragon. There is good agreement between two measurements at 0.500 MeV/u, but a small difference at 0.325 MeV/u, which might be attributed to gas impurity.

In order to minimize the effect of beam instability during the measurements, I_q, the measured charge intensity, was converted to particle intensity, n_q, and normalized to the scattering rate, C, in the elastic monitor, namely,

$$n_q = \frac{I_q}{qC}. \tag{4}$$

The fraction, F_q, of charge state q, was calculated as

$$F_q = \frac{n_q}{\sum n_q}. \tag{5}$$

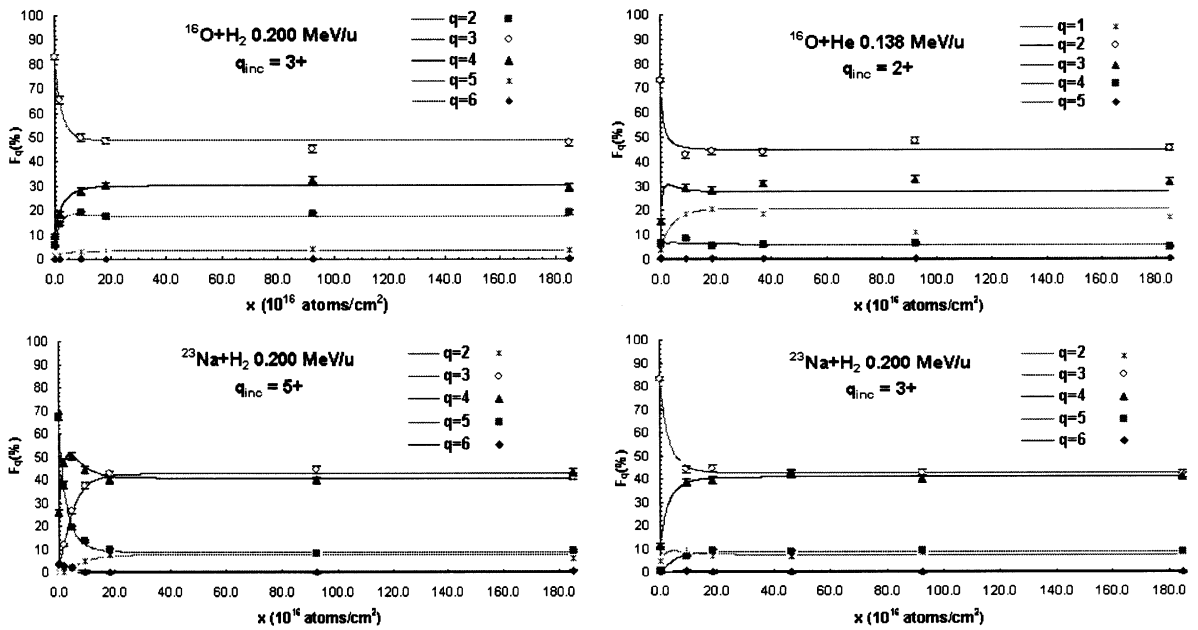

Fig. 5. Fractional charge states distributions measured using the NABONA facility at the University of Naples as a function of target thickness (atoms/cm^2) and incident projectile charge state.

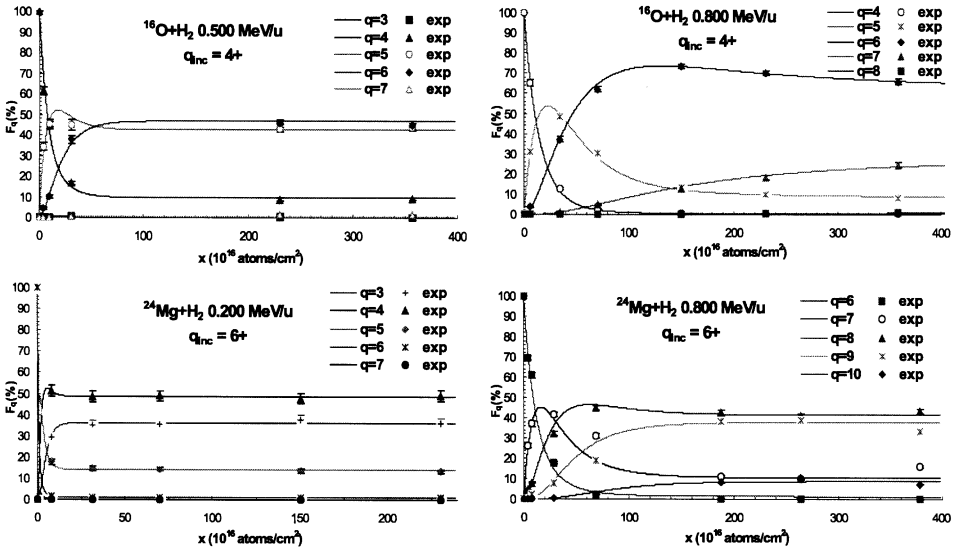

Fig. 6. Fractional charge states distributions measured using the DRAGON target at TRIUMF as a function of target thickness (atoms/cm^2) and incident projectile charge state.

The uncertainty, Δn_q, in n_q can be estimated as

$$\Delta n_q = \sqrt{\left(\frac{\partial n_q}{\partial I_q}\right)^2 (\Delta I_q)^2 + \left(\frac{\partial n_q}{\partial C}\right)^2 (\Delta C)^2} \tag{6}$$

$$= n_q \sqrt{\left(\frac{\Delta I_q}{I_q}\right)^2 + \left(\frac{\Delta C}{C}\right)^2}. \tag{7}$$

The uncertainty, ΔF_q, in the charge state fraction was estimated to be

$$\Delta F_q = \sqrt{\left(\frac{\partial F_q}{\partial n_q}\right)^2 (\Delta n_q)^2 + \sum\nolimits_{q' \neq q} \left(\frac{\partial F_q}{\partial n_{q'}}\right)^2 (\Delta n_{q'})^2} \tag{8}$$

$$= F_q \sqrt{(1-2F_q)\left(\frac{\Delta n_q}{n_q}\right)^2 + \sum\nolimits_{q'} F_{q'}^2 \left(\frac{\Delta n_{q'}}{n_{q'}}\right)^2}. \tag{9}$$

Assuming that each measurement has the same percent error, i.e., all $\Delta n_q/n_q$ are equal to each other, we have

$$\frac{\Delta F_q}{F_q} = \frac{\Delta n_q}{n_q} \sqrt{(1-2F_q) + \sum\nolimits_q F_q^2}. \tag{10}$$

Table 2 presents a more complete error budget.

3.2. Critical thickness

A useful parameter in charge exchange studies with gases is the critical thickness, namely, the target thickness, defined here as where fractions of all charge states are within $\pm 5\%$ of its equilibrium value as listed in Table 1. Table 3 presents these critical target thicknesses and the corresponding pressure. The pressure data from the Naples measurements have also been converted to the pressure of the DRAGON target of the same thickness.

The critical thickness increases as the energy of the projectile increases. Also, comparing the critical thickness x_c of different projectiles with the same velocity passing through hydrogen gas, we noticed that with the increase of the projectile's atomic number, x_c increases slightly. It can also be observed on the growth curves for projectiles of the same species and velocity but different incident charge state that equilibrium is reached relatively faster when the incident charge state is closer to the dominant state at equilibrium. However, additional data is needed to achieve a quantitative empirical description of x_c as a function of Z_p, Z_t, and E.

Table 1
Experimental equilibrium charge state fractions (%), where * and † refer to data from Naples and DRAGON measurements, respectively

	E (MeV/u)	q_{in}	$n(1+)$	$n(2+)$	$n(3+)$	$n(4+)$	$n(5+)$	$n(6+)$	$n(7+)$	$n(8+)$	$n(9+)$	$n(10+)$
$^{15}N + H_2^{\dagger}$	0.435	4+				3.70±0.22	34.32±0.90	57.57±0.95	4.41±0.26			
$^{16}O + H_2^{*\dagger}$	0.138	2+, 3+, 4+	10.46±0.56	43.30±1.21	38.99±1.18	7.01±0.46	0.33±0.05					
$^{16}O + H_2^{*}$	0.200	3+, 4+, 5+		17.59±0.71	48.78±1.21	30.17±1.05	3.41±0.27	0.05±0.01				
$^{16}O + H_2^{*}$	0.325	3+, 5+		1.10±0.09	13.41±0.56	47.59±1.22	34.19±1.13	3.71±0.29				
$^{16}O + H_2^{\dagger}$	0.325	4+			7.37±0.41	50.07±0.94	37.51±0.91	5.05±0.35				
$^{16}O + H_2^{*\dagger}$	0.500	4+			0.50±0.06	10.00±0.44	44.50±1.27	43.50±1.26	1.50±0.09			
$^{16}O + H_2^{\dagger}$	0.500	4+			0.35±0.04	9.89±0.54	41.88±0.95	46.77±0.96	1.11±0.07			
$^{16}O + H_2^{*\dagger}$	0.588	3+			0.11±0.02	3.50±0.29	32.23±1.17	59.85±1.24	4.31±0.30			
$^{16}O + H_2^{\dagger}$	0.800	4+				0.36±0.04	8.93±0.51	65.81±0.84	23.78±0.72	1.12±0.14		
$^{23}Na + H_2^{*}$	0.200	3+, 5+, 6+		7.39±0.49	42.51±1.21	40.78±1.20	8.72±0.57	0.60±0.07				
$^{23}Na + H_2^{*}$	0.374	4+, 6+			1.01±0.11	13.25±0.54	40.90±1.15	34.69±1.09	9.44±0.50	0.71±0.08		
$^{23}Na + H_2^{*\dagger}$	0.478	4+, 7+			0.10±0.02	2.18±0.15	16.74±0.66	40.18±1.14	32.81±1.06	7.50±0.48	0.49±0.08	
$^{24}Mg + H_2^{\dagger}$	0.200	6+			36.17±0.88	48.72±0.94	14.03±0.44	1.07±0.06	0.01±0.001			
$^{24}Mg + H_2^{\dagger}$	0.500	6+				0.66±0.08	8.92±0.40	30.45±0.76	40.81±0.85	17.66±0.51	2.13±0.12	
$^{24}Mg + H_2^{\dagger}$	0.800	6+						1.40±0.08	10.51±0.33	41.64±0.89	37.78±0.86	8.67±0.42
$^{16}O + He^{*}$	0.138	2+, 3+, 4+	20.78±0.79	44.96±1.18	27.69±0.97	6.31±0.35	0.26±0.04					
$^{16}O + He^{*}$	0.200	3+, 4+, 5+	0.02±0.003	33.04±1.10	46.31±1.22	18.64±0.74	1.92±0.15	0.07±0.01				
$^{16}O + He^{*}$	0.325	3+, 5+		7.90±0.43	34.48±1.10	42.28±1.17	14.61±0.59	0.73±0.08				
$^{16}O + He^{*}$	0.371	3+		4.82±0.27	25.56±0.93	47.21±1.47	20.31±0.78	2.10±0.12				
$^{16}O + He^{*}$	0.588	3+			3.90±0.22	24.45±0.90	47.52±1.19	23.31±0.87	0.82±0.09			
$^{16}O + He^{*}$	0.750	6+				9.00±0.59	37.38±1.19	48.11±1.25	5.51±0.31			
$^{16}O + He^{*}$	0.875	5+					29.88±1.11	59.44±1.22	10.68±0.59			

Table 2
Experimental and data analysis uncertainties

Experimental uncertainties—Naples		
Source	Equipment	
Uncertainty		
Pressure	Manometer	4%
Effective target length	Gas cell	3%
Beam charge intensity	Faraday cup	2–10%
Charge state analyzing	Magnet + tuning	2–5%
Experimental uncertainties—DRAGON		
Source	Equipment	
Uncertainty		
Pressure	Manometer	4%
Effective target length	Gas cell	10%
Beam charge intensity	Faraday cup + current integrator	3%
Charge state analyzing	Magnet + reference file	1%
Gas impurity	Target system	5%
Analysis uncertainties		
	Naples	DRAGON
$F(q)<1\%$	10–20%	10%
$1\%<F(q)<10\%$	6–10%	5%
$F(q)>10\%$	4%	3%

3.3. Equilibrium charge state distribution

3.3.1. Gaussian distribution

Fig. 7 presents some of the measured equilibrium charge distributions as a function of different beams and beam energies. These displayed a remarkable symmetry and are well described by a Gaussian distribution dependence as indicated by the solid lines.

Two important parameters, the average equilibrium charge state $\bar{q}$ and distribution width d, are defined as

$$\bar{q} = \sum_q qF_q \tag{11}$$

$$d = \sqrt{\sum_q (q-\bar{q})^2 F_q}. \tag{12}$$

And as a measure of the degree of asymmetry, skewness is introduced and defined as

$$s = \sum_q (q-\bar{q})^3 F_q/d^3. \tag{13}$$

These parameters calculated from experimental data are tabulated together with those from the Gaussian fits in Table 4. The skewness presented indicates the quality of symmetry.

3.3.2. Semi-empirical formulas for $\bar{q}$ and d

The good agreement between experimental results and the Gaussian fits encouraged us to look for semi-empirical equations to describe the average equilibrium charge state and distribution width. In the literature there are several semi-empirical approaches to estimate these average values including [14,15] for solid targets, and the rather complex approach of [16]. The best result (smallest χ^2 value) for our data is based upon on the formulation of Betz et al. [14], which is rearranged here as

$$\bar{q} = Z_p \times \left[1 - \exp\left(-\frac{A}{Z_p^{\gamma}}\sqrt{\frac{E}{E'}} + B\right)\right] \tag{14}$$

where Z_p is the projectile ion atomic number with energy E (MeV/u). To be more comparable with other results, we took $v/(v'Z_p^{\gamma})$ as the reduced velocity with $v' = 3.6\times10^6 i\,\mathrm{m/s}$, instead of $v/(v_0 Z_p^{\gamma})$, where v_0 is the Bohr electron orbital velocity. A was treated as a free parameter along with B and γ (Betz et al. fixed $A=1$ [14]). A value of $E' = 0.067635\,\mathrm{MeV}/u$ corresponding to $v' = 3.6\times10^6\,\mathrm{m/s}$ was used.

The best fit for hydrogen gas targets is reached with $\gamma = 0.44515$, $A = 1.4211$, $B = 0.4495$, and for Helium gas target $\gamma = 0.44515$, $A = 1.1326$, $B = 0.3449$, as shown in Fig. 8(a) and (b). Our experimental data fall nicely on a line with a non-zero y intercept.

Also plotted in Fig. 8(a) are the average equilibrium charge states of low energy ^{16}O passing through hydrogen gas target taken from literature [5]. Despite the good agreement in our energy range, it is clear that for reduced velocity of less than 0.5, which corresponds to a beam energy of less than 0.1 MeV/u for ^{16}O, the experimental data deviate from a linear relation. This indicates that the expression determined cannot be extrapolated to a very low energy region, where $\bar{q}$ goes to zero at zero velocity.

It is not clear why the data point for the data for ^{15}N beam is considerably lower 2+, and 3+ states were not measured. It may be necessary to

Table 3
Critical target thickness x_c and the corresponding pressure at Naples and DRAGON gas target, with* and † referring to data from Naples and DRAGON measurements, respectively

	E (MeV/u)	q_{in}	x_c (10^{16} atoms/cm^2)	P_{NAPLES} (mbar)	P_{DRAGON} (Torr)
$^{15}N + H_2^{\dagger}$	0.435	4+	48.6		0.610
$^{16}O + H_2^{*}$	0.138	2+	7.0	0.038	0.088
		3+	8.1	0.044	0.102
		4+	10.2	0.055	0.128
$^{16}O + H_2^{*}$	0.200	3+	11.6	0.063	0.146
		4+	17.0	0.092	0.214
		5+	19.7	0.106	0.246
$^{16}O + H_2^{*}$	0.325	3+	50.7	0.274	0.637
		5+	44.6	0.241	0.56
$^{16}O + H_2^{\dagger}$	0.325	4+	10.7		0.134
$^{16}O + H_2^{\dagger}$	0.500	4+	77.2		0.969
$^{16}O + H_2^{\dagger}$	0.800	4+	338.1		4.242
$^{23}Na + H_2^{*}$	0.200	3+	14.6	0.079	0.183
		5+	18.3	0.099	0.230
		6+	20.4	0.110	0.256
$^{23}Na + H_2^{*}$	0.374	4+	85.4	0.461	1.071
		6+	63.8	0.341	0.792
$^{23}Na + H_2^{*}$	0.478	4+	140.1	0.757	1.758
		7+	120.6	0.651	1.512
$^{24}Mg + H_2^{\dagger}$	0.200	6+	13.2		0.165
$^{24}Mg + H_2^{\dagger}$	0.500	6+	71.5		0.897
$^{24}Mg + H_2^{\dagger}$	0.800	6+	184.2		2.312
$^{16}O + He^{*}$	0.138	2+	6.47	0.070	0.162
		4+	7.49	0.081	0.188
$^{16}O + He^{*}$	0.200	3+	3.60	0.039	0.091
		4+	6.29	0.068	0.157
		5+	7.97	0.086	0.20
$^{16}O + He^{*}$	0.325	3+	8.69	0.094	0.218
		5+	11.7	0.127	0.295

remeasure this point at a later time when the DRAGON facility and the beam are available. It is interesting to mention that none of the existing semi-empirical formulae in the literature can be used to fit our experimental data without modification.

The distribution width is a very sensitive parameter and no theoretical prediction is available yet.

The charge state distribution width is constant over a wide range (Table 4). Approximately, for the reduced charge state $\bar{q}/Z_p$ in the range of 0.3–0.7, the distribution width can be fitted with the expression

$$d = d_1 Z_p^w \tag{15}$$

with d_1=0.23675 and $w = 0.54772$, respectively.

While plotting the reduced width $d/Z_p^{0.54772}$ versus the average number of electron $\bar{n}_e(= Z_p - \bar{q})$ as suggested by Shima et al. [17], the presence of atomic shell effects become apparent as shown in Fig. 9.

One of the applications of these data are to estimate average charge state distributions for other projectile and target combinations. Fig. 10 displays the measured distribution widths as a

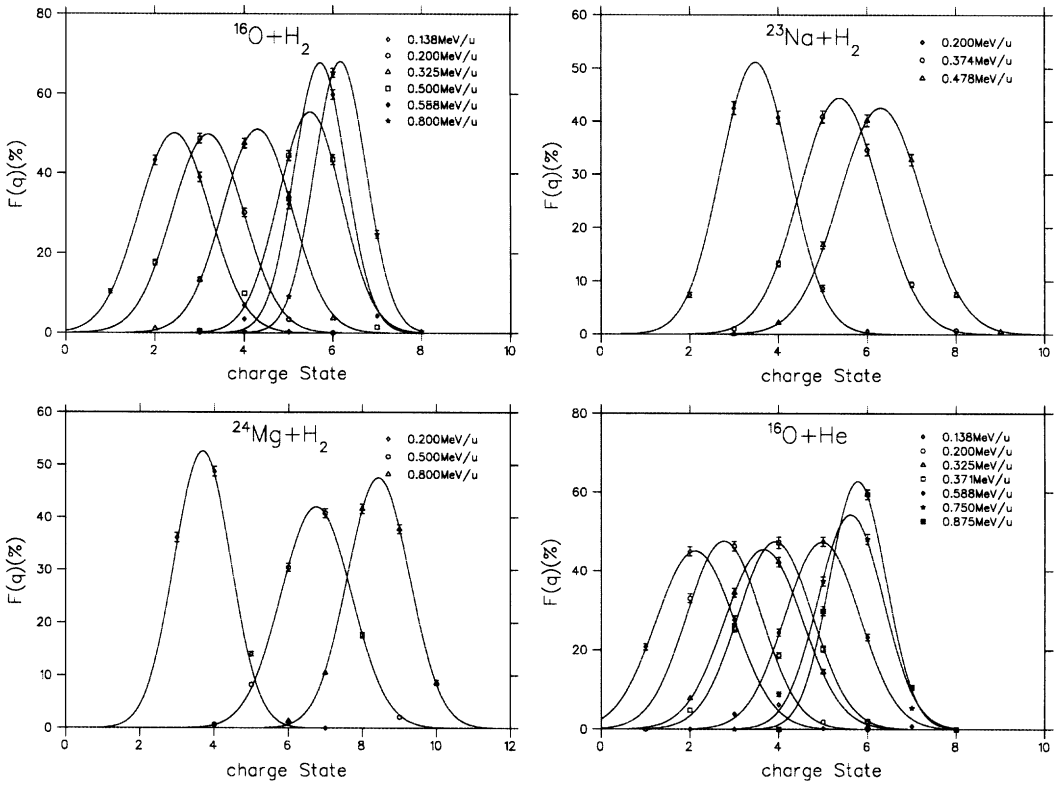

Fig. 7. Equilibrium charge state distribution of ^{16}O, ^{23}Na, ^{24}Mg beam passing through hydrogen gas and ^{16}O beam passing through helium gas, with symbols representing the experimental data and the line indicating the Gaussian distribution fits.

function of average equilibrium distributions and can be used to interpolate such values. Extrapolation would be less accurate (Fig. 11).

3.4. Charge-changing cross-sections

3.4.1. Least-squares methods

The variation of the charge state distribution during the passage through the target can be expressed by a system of linear coupled differential equations as

$$\frac{dF_q}{dx} = \sum_{q',q' \neq q} (F_{q'}\sigma_{q',q} - F_q\sigma_{q,q'}) \tag{16}$$

where F_q is under the restriction

$$\sum_q F_q = 1 \tag{17}$$

Eq. (16) assumes that the ion collisions always occur in their ground state, Eq. (16) assumes that the ion collisions always occur in their ground state, which is appropriate for low energy ions passing through dilute hydrogen and helium gas. The additional restriction to allow only single electron capture and/or loss is also imposed. The least-square method has been adopted to fit the cross-sections from the measured non-equilibrium and equilibrium charge state distributions since the measured fractional distribution curves showed significant deviation from linearity at very low target thickness.

Basically, the least-square sum χ^2 is calculated as

$$\chi^2 = \sum_{q=1}^{q\max} W_q(F_q - Y_q)^2 \tag{18}$$

Table 4
Experimental $\bar{q}$, d, and s versus $\bar{q}$ and d from Gaussian fit, with * and † refer to data from Naples and DRAGON measurements, respectively

	E (MeV/u)	Experimental data			Gaussian distribution	
		$\bar{q}$	d	S	q_{max}	d
$^{15}N + H_2^{\dagger}$	0.435	5.63±0.10	0.629±0.007	−4.00E-5	5.69±0.01	0.603±0.011
$^{16}O + H_2^{*}$	0.138	2.44±0.05	0.784±0.010	9.52E-5	2.43±0.01	0.796±0.004
$^{16}O + H_2^{*}$	0.200	3.20±0.06	0.762±0.010	1.45E-5	3.18±0.01	0.800±0.009
$^{16}O + H_2^{*}$	0.325	4.26±0.08	0.775±0.009	−1.49E-5	4.29±0.01	0.781±0.006
$^{16}O + H_2^{*}$	0.500	5.36±0.10	0.699±0.008	−4.40E-5	5.48±0.02	0.719±0.029
$^{16}O + H_2^{*}$	0.500	5.38±0.08	0.691±0.008	−5.37E-5	5.54±0.04	0.718±0.046
$^{16}O + H_2^{*}$	0.588	5.65±0.10	0.625±0.009	−5.38E-5	5.71±0.02	0.588±0.017
$^{16}O + H_2^{\dagger}$	0.800	6.16±0.08	0.600±0.008	1.32E-5	6.17±0.01	0.586±0.001
$^{23}Na + H_2^{*}$	0.200	3.53±0.07	0.779±0.011	1.87E-5	3.48±0.01	0.780±0.011
$^{23}Na + H_2^{*}$	0.374	5.40±0.10	0.893±0.011	6.55E-6	5.38±0.01	0.897±0.007
$^{23}Na + H_2^{*}$	0.478	6.28±0.11	0.926±0.012	−6.01E-6	6.30±0.01	0.937±0.008
$^{24}Mg + H_2^{\dagger}$	0.200	3.80±0.05	0.711±0.006	4.95E-5	3.68±0.02	0.758±0.021
$^{24}Mg + H_2^{\dagger}$	0.500	6.73±0.09	0.940±0.009	−7.30E-6	6.75±0.01	0.949±0.006
$^{24}Mg + H_2^{\dagger}$	0.800	8.42±0.12	0.843±0.008	−1.84E-5	8.44±0.01	0.839±0.005
$^{16}O + He^{*}$	0.138	2.20±0.04	0.848±0.010	3.24E-5	2.12±0.02	0.885±0.011
$^{16}O + He^{*}$	0.200	2.90±0.05	0.768±0.009	4.68E-5	2.77±0.03	0.838±0.024
$^{16}O + He^{*}$	0.325	3.66±0.07	0.848±0.010	9.37E-7	3.66±0.01	0.877±0.005
$^{16}O + He^{*}$	0.371	3.89±0.08	0.851±0.010	−5.95E-6	3.92±0.01	0.841±0.008
$^{16}O + He^{*}$	0.588	4.93±0.09	0.813±0.010	−2.10E-5	4.98±0.01	0.842±0.008
$^{16}O + He^{*}$	0.750	5.50±0.10	0.735±0.011	−2.68E-5	5.62±0.03	0.735±0.034
$^{16}O + He^{*}$	0.875	5.81±0.10	0.607±0.009	1.23E-5	5.78±0.01	0.635±0.005

where F_q and Y_q are the experimental charge fractions and those from numerical integration of Eq. (16). W_q is the weighing factor chosen with respect to the experimental uncertainty in F_q. The sum runs over the charge fractions measured for all charge states and target thicknesses for specific projectile and target combination. The cross-sections are determined by minimizing χ^2, regarding all cross-sections as free parameters.

All fitted cross-sections with uncertainties are tabulated in Tables 5 and 6. Figs. 5 and 6 display some of the fits which are in excellent agreement between the calculated growth curves and the data point. In cases when χ^2 per degree of freedom is larger than 1, the uncertainties have been multiplied by the square root of χ^2 per degree of freedom. Since the non-equilibrium charge state distribution depends on the target thickness, an additional error was introduced by the uncertainty of the target effective length. This affects all the fitted cross-sections by $\pm 10\%$. The agreement of the growth curves calculated from these cross-sections with the experimental data indicates that the model of a single electron capture and loss is a reasonable assumption. In the growth curves corresponding to large differences between incident and equilibrium charge states (see, e.g., Mg beam of 0.2 MeV/u and 6^+ charge state passing through hydrogen gas as shown in Fig. 6) the sharp peaks observed for intermediate charge states nicely indicate the multistep one-electron exchange nature of the process.

The fitted charge-changing cross-sections related to charge states with low fraction F_q (say, less than 1%) have large uncertainties because of the large uncertainties associated with the measured F_q. This occurs mainly for charge states well removed either from the incident charge state or the

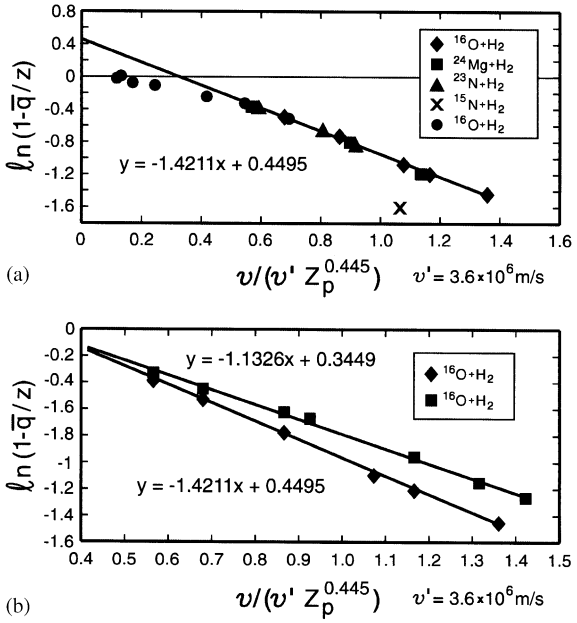

Fig. 8. Presented here is $\ln(1-\bar{q}/z)$ plotted as a function of reduced velocity for different beams in hydrogen and helium. In (a) the data (solid circles) for the O beam at low velocities are taken from the literature [5].

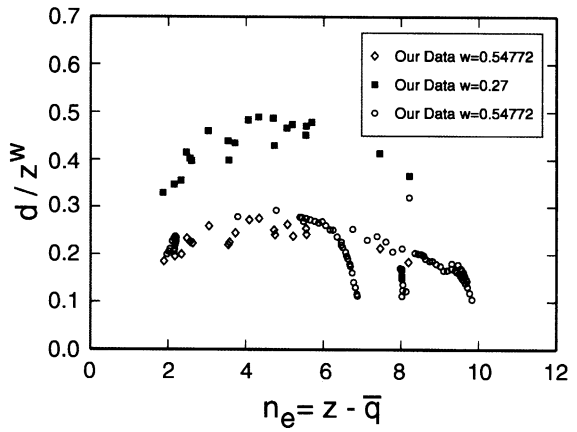

Fig. 9. Reduced width $d/(Z_p^w)$ plotted as a function of mean number of electrons $n_e(=Z_p-\bar{q})$.

equilibrium state. Improvement of this situation requires further studies with incident beams in these charge states, which were not available for this study. However for practical purposes these oases are not important. Further, in situations in which insufficient non-equilibrium distributions were measured, the charge exchange cross-sections are not well determined.

Limited by little published data available for direct comparison, we extrapolated data from Montenegro et al. [18] on $\sigma_{5,6}$ and $\sigma_{5,4}$ of oxygen beam passing through hydrogen, as shown in Table 7. Their data of cross-sections have been fitted to single power law, e.g.,

$$\sigma_{5,6} = aE^{\beta} \tag{19}$$

where a and β are free parameters. Then, corresponding cross-sections for 0.138 and 0.200 MeV/u ^{16}O beam passing through hydrogen and helium gas have been calculated and are listed in Table 7 with our experimental data. Their cross-sections with hydrogen gas in units of cm^2/molecule have been converted to units of cm^2/atom, as a hydrogen molecule contains two atoms. Comparison with our data indicates good agreement. Other than this, we are not aware of any published data with which to compare the present measurements.

3.4.2. Scaling rules for charge-changing cross-sections

Charge-changing cross-sections are functions of projectile atomic number Z_p, target atomic number Z_t, ion charge state q and energy E. Following the application of a simplified theoretical model, which gives simple power functions for the dependence of cross-sections on these parameters, we checked the dependence of the cross-sections on q and E, respectively, as shown in Fig. 11 for oxygen beam passing through hydrogen for example.

Because of the diversity in the dependence of these cross-sections on the all the parameters, no universal fit as that described by Berkner et al. [19] can be achieved from our data.

4. Summary/conclusions

A windowless gas target followed by an analyzing magnet has been used at the University of Naples and at TRIUMF to study the charge state distribution of ions passing through hydrogen or

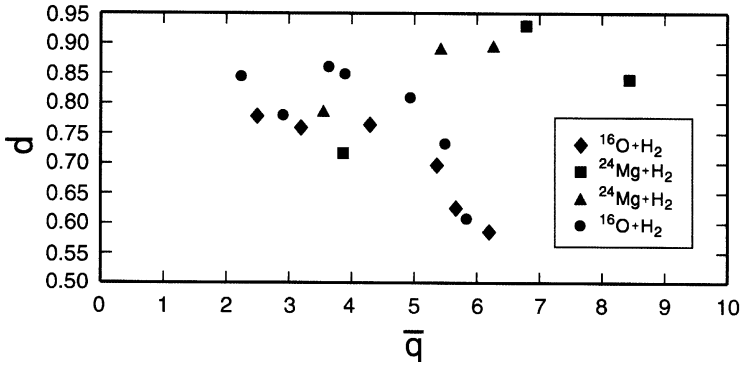

Fig. 10. Distribution width d plotted as a function of relative average equilibrium charge state. The errors are the size of the points.

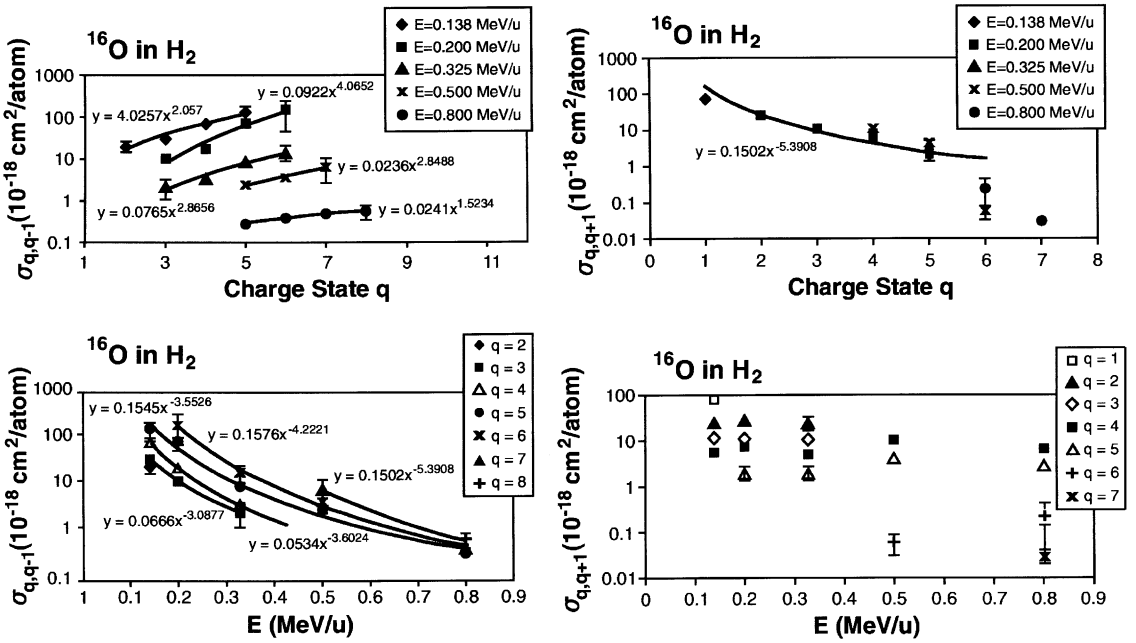

Fig. 11. Single electron capture (on left) and single electron capture cross-sections of ^{16}O beam passing through H_2 gas as a function of charge state, q, and projectile energy, E, respectively.

helium gas. The data will be essential in the interpretation of radiative capture experiments at energies of interest in nuclear astrophysics.

We have measured charge state distributions not presently available in the literature, and also developed semi-empirical formulas for estimating average equilibrium charge states and distribution widths for low energy heavy ion passing through hydrogen and helium gas targets. These formulas are useful in predicting equilibrium charge state distributions within the energy range from 0.138 to 0.875 MeV/u. Extrapolation beyond this range is not recommended.

Charge changing is a complicated many-body collision process, and a theory is not yet available to predict the distribution accurately. In such a situation, semi-empirical formulas have been developed and are useful but are limited to a

Table 5
Single electron capture and loss cross-sections for heavy ions, with * and † referring to data from Naples and DRAGON measurements, respectively

	E (MeV/u)	Single electron capture			Single electron loss		
		q	q'	$\sigma_{q,q'}$ (10^{-18} cm^2)	q	q'	$\sigma_{q,q'}$ (10^{-18} cm^2)
$^{16}O + H_2^*$	0.138	2	1	19.6±5.2	1	2	81.0±20.8
		3	2	29.4±4.1	2	3	26.5±3.6
		4	3	68.1±3.3	3	4	12.2±1.9
		5	4	126.6±46.3	4	5	5.9±0.7
$^{16}O + H_2^*$	0.200	3	2	10.0±1.0	2	3	27.8±3.5
		4	3	17.1±2.3	3	4	10.6±1.5
		5	4	69.5±11.2	4	5	7.9±0.8
		6	5	150.1±105.5	5	6	2.1±0.7
$^{16}O + H_2^*$	0.325	3	2	2.1±1.1	2	3	25.1±8.0
		4	3	3.1±0.3	3	4	11.2±0.6
		5	4	7.5±0.6	4	5	5.4±0.5
		6	5	14.8±5.8	5	6	2.0±0.6
$^{16}O + H_2^\dagger$	0.500	5	4	2.4±0.3	4	5	10.4±0.6
		6	5	3.6±0.6	5	6	4.1±0.3
		7	6	6.3±3.8	6	7	0.06±0.03
$^{16}O + H_2^\dagger$	0.800	5	4	0.27±0.04	4	5	6.8±0.2
		6	5	0.38±0.03	5	6	2.7±0.2
		7	6	0.50±0.07	6	7	0.23±0.02
		8	7	0.54±0.22	7	8	0.03±0.01
$^{23}Na + H_2^*$	0.200	3	2	4.8±0.4	2	3	27.7±2.5
		4	3	15.7±0.8	3	4	15.1±0.8
		5	4	37.7±1.7	4	5	8.1±0.5
		6	5	66.8±4.3	5	6	4.6±0.5
$^{23}Na + H_2^*$	0.374	4	3	1.4±0.4	3	4	17.9±5.7
		5	4	2.1±0.2	4	5	6.7±0.4
		6	5	5.3±0.5	5	6	4.8±0.4
		7	6	10±2.4	6	7	2.7±0.5
		8	7	15.1±10.2	7	7	0.84±0.14

Uncertainties of the cross-sections have been normalized to make χ^2 per freedom be 1.0. Additional normalization of all the cross-sections with respect to the uncertainty in the target effective length are not included here.

certain range. We found that none of the empirical or semi-empirical formulas published previously can be applied to our case directly.

Charge-changing cross-sections provide the basis for a complete description of the charge state distribution resulting from ion–atom encounters. While some cross-sections have been estimated from our distribution data, further studies would be required to understand completely the charge-changing processes of low energy heavy ions passing through hydrogen and helium gas.

Acknowledgements

The efforts of Jan Soukup and Roland Kokke in the design of the gas target are acknowledged. The creative efforts of Dennis Healey in all aspects of

Table 6
Single electron capture and loss cross-sections for heavy ions, with * and † referring to data from Naples and DRAGON measurements, respectively (continued)

	E (MeV/u)	Single electron capture			Single electron loss		
		q	q'	$\sigma_{q,q'}$ (10^{-18} cm^2)	q	q'	$\sigma_{q,q'}$ (10^{-18} cm^2)
$^{23}Na + H_2^*$	0.478	4	3	0.67±0.26	3	4	14.8±8.1
		5	4	0.72±0.17	4	5	6.7±0.6
		6	5	1.8±0.2	5	6	4.4±0.6
		7	6	3.6±0.6	6	7	2.7±0.2
		8	7	4.3±1.9	7	8	1.1±0.2
		9	8	11.9±10.8	8	9	0.64±0.2
$^{24}Mg + H_2^\dagger$	0.200	4	3	17.7±0.2	3	4	24.1±0.3
		5	4	55.2±0.6	4	5	16.1±0.6
		6	5	97.2±0.6	5	6	7.1±0.2
$^{24}Mg + H_2^\dagger$	0.500	5	4	3.0±0.6	4	5	37.6±6.6
		6	5	4.8±0.9	5	6	18.3±6.0
		7	6	4.8±1.6	6	7	6.9±0.9
		8	7	10.1±0.6	7	8	4.4±0.3
		9	8	12.5±0.6	8	9	1.7±1.4
$^{24}Mg + H_2^\dagger$	0.800	7	6	1.1±0.3	6	7	8.1±0.5
		8	7	1.2±0.4	7	8	4.8±0.5
		9	8	2.6±0.5	8	9	2.4±0.5
		10	9	3.0±2.0	9	10	0.75±0.30
$^{16}O + He^*$	0.138	2	1	15.5±4.5	1	2	33.5±11
		3	2	127±8	2	3	78±6
		4	3	218.0±75	3	4	50±18
		5	4	360±200	4	5	15±10
$^{16}O + He^*$	0.200	3	2	48.8±6.0	2	3	68.4±10.8
		4	3	69.8±12.3	3	4	28.1±4.8
		5	4	154±29	4	5	16±3
		6	5	292.1±173.9	5	6	10.0±8.9
$^{16}O + He^*$	0.325	3	2	16.0±1.5	2	3	69.7±7.0
		4	3	31.0±2.2	3	4	38.0±2.2
		5	4	41.0±6.3	4	5	14.2±1.9
		6	5	136.1±10.4	5	6	6.8±0.5

Uncertainties of the cross-sections have been normalized to make χ^2 per freedom be 1.0. Additional normalization of all the cross-sections with respect to the uncertainty in the target effective length are not included here.

the original development of the hydrogen gas recirculation trap and other aspects of the estimated performance of the target are greatly appreciated. The assistance of Hart Sprenger, and the TRIUMF Beam Line group in the assembly of the gas target are also acknowledged. The project could not have been performed without considerable efforts of Bob Laxdal and Matteo Pasini in the operation of the TRIUMF-ISAC accelerator and the Naples group including Enzo Roca and Luigi Campajola for the operation of the University of Naples Van der Graaf accelerator. The financial support received from the Natural Science and Engineering Research Council of

Table 7
Comparison of charge-changing cross-sections for O^{5+} in H_2 and He with literature [18]

Cross-section data from Montenegro et al.				
E (MeV)	H_2 target		He target	
	$\sigma_{5,6}(10^{-18}\,cm^2)$	$\sigma_{5,4}(10^{-18}\,cm^2)$	$\sigma_{5,6}(10^{-18}\,cm^2)$	$\sigma_{5,4}(10^{-18}\,cm^2)$
2.0	1.6 ± 0.2	597 ± 66	1.2 ± 0.1	448 ± 54
2.5	2.4 ± 0.2	283 ± 31	2.4 ± 0.3	289 ± 35
3.0	3.7 ± 0.4	241 ± 29	3.3 ± 0.4	229 ± 27
3.5	4.1 ± 0.4	107 ± 1.2	4.2 ± 0.5	183 ± 22
4.0	5.2 ± 0.5	50.4 ± 5.5	5.3 ± 0.6	91.2 ± 11

Extrapolated data compared to present experimental data				
E (MeV/u)	H_2 target			
	$\sigma_{5,6}(10^{-18}\,cm^2)$		$\sigma_{5,4}(10^{-18}\,cm^2)$	
	Extrapolated data	Our data	Extrapolated data	Our data
0.138			$242.0\pm10\%$	126.6 ± 46.3
0.200	$1.83\pm10\%$	2.1 ± 0.7	$67.6\pm10\%$	69.5 ± 11.2
E (MeV/u)	He target			
	$\sigma_{5,6}(10^{-18}\,cm^2)$		$\sigma_{5,4}(10^{-18}\,cm^2)$	
	Extrapolated data	Our data	Extrapolated data	Our data
0.137			$395.2\pm10\%$	357.1 ± 191.5
0.200			$177.3\pm10\%$	154.3 ± 28.3

Canada is also gratefully acknowledged. U.G. was supported by a Department of Energy grant (DE-FG03-93ER40789). S.E. wishes to acknowledge support from the Deutsche Forschungsgemeinschaft (DFG GR 1577-301). Support by a US DOE Grant No. DE-FG02-91ER-40609 is also acknowledged.

References

[1] J.M. D'Auria, L. Buchmann, D. Hutcheon, P. Lipnik, D. Hunter, J. Rogers, R. Helmer, U. Giesen, A. Olin, P. Bricault, N. Bateman, Nucl. Instr. and Meth. B 126 (1997) 262.
[2] J.M. D'Auria for the DRAGON Collaboration, astrophysics with a DRAGON at ISAC, Nucl. Phys. A 701 (2002) 625c.
[3] D. Hutcheon, et al., The DRAGON facility for nuclear astrophysics at TRIUMF–ISAC: design, construction and operation, Nucl. Instr. and Meth., submitted.
[4] H.D. Betz, Rev. Mod. Phys. 44 (1972) 465.
[5] A.B. Wittkower, H.D. Betz, At. Data 5 (2) (1973) 113.
[6] W.K. Wu, B.A. Huber, K. Wiesemann, At. Data Nucl. Data Tables 42 (1989) 157.
[7] A. Wiebert, B. Erlandsson, R. Hellborg, K. Stenström, G. Skog, Nucl. Instr. and Meth. A 366 (1995) 17.
[8] L. Campajola, et al., Nucl. Instr. and Meth. B 29 (1987) 129.
[9] F. Terrasi, et al., Nucl. Instr. and Meth. B S2 (1990) 259.
[10] L. Gialanella, et al., Nucl. Instr. and Meth. A 376 (1996) 174.
[11] R.E. Laxdal, et al., The RNB post-accelerator for ISAC at TRIUMF—present and future, Nucl. Phys. 701 (1–4) (2002) 647.
[12] R.E. Laxdal, Completion and operation of ISAC-I and extension to ISAC-II, Proceedings of 2001, Particle Accelerator Conference, Chicago, USA, June 2001.
[13] Wenjie Liu, Charge state studies of heavy ions passing through gas, M.Sc. Thesis, Simon Fraser University, 2001.

[14] H.D. Betz, G. Hortig, E. Leischner, Ch. Schmelzer, B. Stadler, J. Weihrauch, Phys. Lett. 22 (1966) 643.
[15] V.S. Nikolaev, I.S. Dmitriev, Phys. Lett. A 28 (1968) 277.
[16] G. Schiwietz, P.L. Grande, Nucl. Instr. and Meth. B 175 (2001) 125.
[17] K. Shima, N. Kuno, I.S. Dmitriev, Phys. Rev. 40 (1989) 3557.
[18] E.C. Montenegro, G.M. Sigaud, Phys. Rev. A 45 (1992) 1575.
[19] K.H. Berkner, W.G. Graham, R.V. Pyle, A.S. Schlachter, J.W. Steams, Phys. Rev. A 23 (1992) 2891.